

Highly durable electrocatalyst with low-loading platinum-cobalt nanoparticles dispersed over single-atom Co-N-Graphene nanofiber for efficient fuel cell

Lina Chong (✉ chonglina@anl.gov)

Argonne National Laboratory <https://orcid.org/0000-0002-2061-6916>

Jianguo Wen

Argonne National Laboratory <https://orcid.org/0000-0002-3755-0044>

Zhenzhen Yang

Argonne National Laboratory

Yulin Lin

Argonne National Laboratory

Ira Bloom

Argonne National Laboratory

Daniel Abraham

Argonne National Laboratory <https://orcid.org/0000-0003-0402-9620>

Article

Keywords: Highly durable electrocatalyst, low-loading platinum-cobalt nanoparticle, Co-N-Graphene nanofiber, efficient fuel cell

Posted Date: April 1st, 2021

DOI: <https://doi.org/10.21203/rs.3.rs-347344/v1>

License:  This work is licensed under a Creative Commons Attribution 4.0 International License.

[Read Full License](#)

1 Highly durable electrocatalyst with low-loading platinum-cobalt
2 nanoparticles dispersed over single-atom Co-N-Graphene nanofiber for
3 efficient fuel cell

4

5 Lina Chong^{1,*}, Jianguo Wen^{2,*}, Zhenzhen Yang¹, Yulin Lin², Ira D. Bloom¹, Daniel
6 Abraham^{1,*}

7 ¹Chemical Sciences and Engineering Division, Argonne National Laboratory, Argonne, IL 60439, USA;

8 ²Center for Nanoscale Materials, Argonne National Laboratory, Argonne, IL 60439, USA;

9 *Email: chonglina@anl.gov; jwen@anl.gov; abraham@anl.gov,

10

11 Development of highly-active, durable and cost-effective oxygen reduction electrocatalyst for
12 proton exchange membrane fuel cell is crucial and greatly desired to enable fuel cell powered
13 vehicles that are competitive with internal combustion engine automobiles. The support's
14 structure is known to strongly influence the performance of Pt particles. Here, we present a new
15 catalyst containing PtCo core-shell nanoparticle supported over hierarchical tailored porous
16 carbon nanofibers with densely populated single-atomic Co-Nx sites embedded in N-doped
17 graphene. In a fuel cell with a total Pt loading (anode + cathode) of 0.091 mg cm⁻², the new
18 catalyst delivered unprecedented mass activity of 2.28 A mg_{Pt}⁻¹ at 0.9 V_{iR-free}, Pt utilization of
19 11.1 kW g_{Pt}⁻¹ at 150 kPa_{abs}, and high durability with 80% retention of initial mass activity after
20 30,000 accelerated-stress-test cycles, significantly higher than that of the state-of-the-art
21 Pt₃Co/C. In-situ X-ray absorption spectroscopy revealed structure reversibility of the catalyst

22 during oxygen reduction reaction and indicated that the enhanced activity can be attributed to
23 simultaneous PtCo and Co-N_x contributions.

24

25 Proton Exchange Membrane Fuel Cells (PEMFCs) are considered a promising high-efficiency,
26 clean energy technology having a theoretical specific energy sufficient for transportation and
27 stationary applications¹⁻³. The four-electron transfer oxygen reduction reaction (ORR) at the
28 cathode is paramount for fuel cell operation, and its sluggish kinetics, which is six orders of
29 magnitude lower than the hydrogen oxidation reaction at the anode, limits overall performance of
30 the PEMFC^{3,4}. The Pt usage of a commercial fuel cell powered vehicle is 30 g per stack, which is
31 substantially higher than the 2-8 g_{Pt} in incumbent internal combustion engine (ICE) vehicles, and
32 far from the long term sustainability target of < 5 g_{Pt} per vehicle⁵. To compete with ICE vehicles,
33 the total Platinum-group-metal (PGM) loading, including anode and cathode on the membrane
34 electrode assembly (MEA), should be restricted to less than 0.125 mg_{Pt} cm⁻², giving 8 g of PGM
35 per vehicle. Designing highly active, durable and cost-effective electrocatalysts, to boost ORR
36 and reduce the Pt consumption without compromising performance in a fuel cell, is challenging
37 and critical for the widespread commercial application of PEMFC^{3,6}.

38 The widely used Pt catalysts are loaded on carbon supports with high surface area and high
39 porosity to enable sufficient increase of Pt mass-specific surface area and to secure enough pores
40 for reactant O₂ gas to access Pt, thus ensuring maximum mass activity. It is believed that Pt
41 nanoparticles (NPs) are located in the interior of the micropores⁷ (pore diameter < 2 nm) of the
42 high surface area carbon, which enhance the Pt mass activity but restrict its direct contact with
43 ionomer and reactant gas at low voltage, therefore hindering its performance at high current
44 density. While, pore diameter of 4-7 nm for Pt deposition facilitates Pt to achieve both excellent

45 ORR activity and mass transport property⁸. To further improve the Pt ORR activity, one can
46 introduce PGM-free ORR catalyst as support for Pt to replace the conventional carbon forming a
47 synergistic catalyst. For example, in our previous work, we synthesized synergistic catalysts
48 where high surface area Co-N-C PGM-free catalyst was used as support for low loading PtCo
49 alloy (LP@PF)⁴. The LP@PF presented an extraordinarily high Pt mass activity up to 1.77 A
50 mg_{Pt}⁻¹ in a H₂-O₂ PEMFC.

51 In addition to activity, the high durability is another criterion for evaluation of an efficient
52 ORR catalyst. For both PGM and PGM-free catalysts, carbon corrosion and demetallation are the
53 two main factors leading to fast degradation of catalyst performance⁹. Increasing the carbon
54 graphitization, strengthening the anchoring effect between Pt NPs and the support, coating Pt
55 NPs with protecting layers are effective approaches for Pt to achieve sustained stability¹⁰. In a
56 catalyst, micropores host the active site¹¹ (e.g. Co-N₄), and mesopores govern the mass transfer
57 and ionomer distribution. Therefore, to maximize the Pt performance in term of activity and
58 stability by introducing PGM-free catalyst as support, a rational design of the PGM-free catalyst
59 with high surface area, balanced micro- and meso- (pore size 2 nm - 50 nm) porosity, excellent
60 corrosion resistance, electron conductivity, and strong affinity to Pt NPs, is essential^{4,9}.
61 Additionally, in an ideal PGM-free catalyst, within each micropore, a dense population of active
62 sites should be freely accessible to the reactant and product. And the meso-/macro-pores should
63 offer minimal transport resistance and be interconnected through a robust, continuous conductive
64 matrix. As a consequence, the accessibility of reactant to the active sites is enhanced, giving rise
65 to the excellent electrocatalytic activity for PGM-free catalyst toward ORR^{4,12-14}.

66 In this work, we introduce a new design of a low loading PtCo catalyst (LPCNGF), where a
67 Co-N-graphene nanofiber (Co-N-GF) PGM-free catalyst is used as support for PtCo core-shell

68 alloy NP. The newly developed Co-N-GF possesses high surface area, hierarchical pore
69 structures, high density of atomically dispersed Co-Nx, and N-doped graphene, which result in
70 the new LPCNGF catalyst achieving the highest Pt mass activity and sustained electrode
71 stability. Cobalt zeolite imidazole framework, a member of the metal organic framework (MOF;
72 Co-MOF) family, was selected for this study as the source for Co-Nx active site formation¹⁵.
73 Also, it served as the metallic Co source which was the nucleation center for further PtCo alloy
74 synthesis⁴. We chose PtCo alloy because the ordered core@shell structured PtCo alloy with ~3
75 layers of Pt shell demonstrated remarkable activity and stability among PGM NPs¹⁶.
76 Polyacrylonitrile (PAN) was selected as the polymer for fabrication of nanofiber containing Co-
77 MOF, as PAN fiber is known as the chemical precursor of a high-quality carbon fiber. PAN can
78 be converted to n-type N-doped graphene possessing excellent electron conductivity and
79 corrosion resistance through high temperature pyrolysis¹⁷. Moreover, carbon surface modified
80 with N-functional groups facilitate the homogenous distribution of ionomer, resulting in
81 enhanced Pt utilization, thus high current density at low voltage¹⁸. The use of Co-MOF and PAN
82 here not only promise a high-quality graphene with hierarchical pore structure, but also a high
83 concentration and uniform distribution of Co-Nx sites and nitrogen sites throughout the carbon
84 surface, which can further enhance catalyst performance¹⁸. The catalyst exhibits a high mass
85 activity of $5.08 \text{ A mg}_{\text{Pt}}^{-1}$ at 0.9 V measured in a rotating disk electrode experiment, which is 52
86 and 13 times that of Pt/C and the state-of-the-art Pt₃Co/C (umico), respectively. In a H₂-O₂
87 PEMFC cell with total Pt loading (anode + cathode) of 0.091 mg cm⁻², LPCNGF achieved
88 unprecedented mass activity of $2.28 \text{ A mg}_{\text{Pt}}^{-1}$ at 0.9 V_{iR-free}, and Pt utilization of $11.1 \text{ kW g}_{\text{Pt}}^{-1}$ at
89 150 kPa_{abs}, which rank the highest among the reported (Supplementary Table 3). The catalyst
90 was highly stable which retained 80% of initial mass activity after 30,000 accelerated stress test

91 cycles. The synergistic oxygen reduction reaction was studied by performing operando X-ray
92 absorption spectroscopy experiments.

93

94 **Results and Discussion**

95 **Synthesis and characterization of LPCNGF catalyst.** Co-MOF was first fabricated into
96 interconnected nanofiber by electrospinning its mixture with PAN (Supplementary Fig. 1a). The
97 obtained fiber mat was subjected to heat treatment at 1000 °C for 1.5 h under Ar atmosphere.
98 After pre-leaching in 0.5 M H₂SO₄, the obtained Co-N-GF was used as support and nucleation
99 center for the *in-situ* reduced Pt NPs. A second heat treatment under NH₃ was performed as the
100 final step of the catalyst synthesis. The synthesis process is schematically shown in Fig. 1a. The
101 optimizations of LPCNGF are shown in the Supplementary Fig. 2-5. The NH₃ was used as an
102 additional nitrogen precursor, as NH₃ gasifies the disordered domains of the carbon, I) creating
103 micropores into the support; II) producing N-bearing functionalities to bind cobalt cations
104 forming Co-N_x sites; III) generating n-type graphene by donating electrons to graphene¹⁹,
105 facilitating ORR²⁰. The created nitrogen functional groups interact with the ionomer chain,
106 promoting homogeneous distribution of ionomer throughout the catalyst layers^{18,21}. The catalyst
107 achieved a surface area of 824.7 m² g⁻¹ (Supplementary Fig. 4c), as determined by the Brunauer-
108 Emmett-Teller (BET) method. The pore size analysis indicates a high volume of micropores, and
109 appropriate volume of meso-/macro-pores in Co-N-GF (Fig. 1b, Supplementary Table 1-2).
110 Raman spectrum (Fig. 1c) confirms the graphene nature of the carbon fiber as evidenced by the
111 peaks at 2653 cm⁻¹ and 2915 cm⁻¹ corresponding to 2D-band and D+G-band of graphene²².
112 The catalyst has an interconnected network structure, with “beads” lining up on the “string” (
113 Fig. 2a, Supplementary Fig. 1b-1c). The “beads” were converted from Co-MOF, maintaining

114 MOF-like morphology with hollowed structure. High-angle annular dark-field scanning
115 transmission electron microscopy (HAADF-STEM) images, combined with energy-dispersive
116 X-ray spectroscopy (EDS) element mapping, revealed the formation of PtCo alloy and
117 homogenous distribution of N in the carbon matrix (Fig. 2**b**-**c**, 2**e**). The average particle size
118 was ~ 3 nm (Supplementary Fig. 1**d**, 1**e**). The formation of PtCo alloy was further confirmed by
119 X-ray Diffraction (XRD) (Supplementary Fig. 6). The atomic ratio of Co:N:Pt:C was
120 1.6:4.0:0.4:94 determined by EDS (Supplementary Fig. 7). Atomic-resolution HAADF-STEM
121 revealed the dense atomically-dispersed Co embedded in the carbon matrix, and the bright dots
122 are assigned to Co based on electron energy-loss spectroscopy (EELS) results (Fig. 2**d**,
123 Supplementary Fig. 8). EELS also revealed the co-existence of N with Co, suggesting Co-N_x
124 populations, which are the active sites in PGM-free catalysts²³. High-resolution TEM (HRTEM)
125 indicated that the carbon mainly consisted of graphene sheets, with ~ 0.35 nm d-spacing of the
126 (002) basal plane in both “beads” and “string” (Fig. 2**f**, Supplementary Fig. 1**f**). This value is
127 larger than the d-spacing of well-ordered graphite (0.34 nm), suggesting the incorporation of N
128 into the graphitic structure. The carbon contains plenty of mesopores (Fig. 2**f**, Supplementary
129 Fig. 1f). Co-N-GF possesses high BET surface area, hierarchical tailored porosity, homogenous
130 distributed Co-N_x, and plenty of N-doped graphene, a high ORR activity and durability with
131 optimized mass transport property can be expected. HRTEM image also revealed that the PtCo
132 alloy had a core-shell structure: 2 ~ 3 atomic layers of Pt shell and the ordered PtCo alloy core
133 (Fig. 2**g**). The Pt shell was strained and partially covered with CoN_x/C terraces (Fig. 2**g**,
134 Supplementary Fig. 9), which could protect Co/Pt against leaching under the high voltage harsh
135 operating conditions in the fuel cell⁴.

136

137 **Electrocatalytic performance evaluation.** Rotating ring-disk electrode (RRDE) testing in
138 oxygen saturated 0.1 M HClO₄ revealed a half-wave potential of 0.93 V (vs. RHE) for LPCNGF
139 (Fig. 3a). The average number of transferred electrons per O₂ molecule (ne) was 3.94~3.99,
140 corresponding to a low H₂O₂ yield of < 3% (Fig. 3b). The Pt/C and the state-of-the-art Pt₃Co/C
141 catalyst from Umicore (Pt₃Co/C(Um)) were tested under the same condition as benchmarks.
142 Even with higher Pt loading in Pt/C and Pt₃Co/C(Um) than that in LPCNGF, the half-wave
143 potential of Pt/C and Pt₃Co/C(Um) were 0.86V and 0.91 V, 70 mV and 20 mV lower than that of
144 LPCNGF (Fig. 3a), respectively. Tafel plots of mass activities obtained from Fig. 3a normalized
145 by the total mass of the loaded Pt, exhibited a slope of 63 mV dec⁻¹ for LPCNGF (Fig. 3c),
146 smaller than that of Pt/C (89 mV dec⁻¹) and Pt₃Co/C(Um) (71 mV dec⁻¹), suggesting the better
147 ORR kinetics for the former. Furthermore, the LPCNGF displayed a mass activity (MA) of 5.08
148 A mg_{Pt}⁻¹ at 0.9 V, 52 and 13 times higher than that of Pt/C (0.098 A mg_{Pt}⁻¹) and Pt₃Co/C(Um)
149 (0.39 A mg_{Pt}⁻¹), respectively. The high mass activity of LPCNGF in the kinetic range (voltage >
150 0.8 V) ranks it among the best ORR catalysts (Supplementary Table 3). The MA and specific
151 activity (SA) retain ~ 90% of the initial values, with only 6 mV loss in half-wave potential after
152 10,000 potential cycles, demonstrating the high durability of LPCNGF in acid (Fig. 3d,
153 Supplementary Fig. 10c).

154 The high ORR activity measured through RRDE does not directly reflect the performance in a
155 practical fuel cell due to the fundamentally different operating conditions, e.g. temperature,
156 electrolyte, electrode structure, etc. To measure its fuel cell performance, we integrated LPCNGF
157 into a MEA, evaluated its performance in an operating PEMFC including H₂-Air and H₂-O₂ cells
158 (Supplementary Fig. 11-12), and benchmarked to Pt₃Co/C(Um). For comparison, the Pt loading
159 at cathode and anode for all the MEAs were $\leq 0.056 \text{ mg}_{\text{Pt}} \text{ cm}^{-2}$ and $\leq 0.035 \text{ mg}_{\text{Pt}} \text{ cm}^{-2}$,

160 respectively. For each test, MEA was manufactured and tested for reproducibility purpose for at
161 least 3 times. Fig. 4a shows H₂-Air cell performance at 200 kPa_{abs}. The current-voltage
162 polarization profile of LPCNGF is dramatically higher than that of Pt₃Co/C(Um) throughout the
163 entire polarization curve. In addition, the current density at 0.8 V is 438 mA cm⁻² for LPCNGF, 4
164 times larger than that of Pt₃Co/C(Um) (106 mA cm⁻² at 0.8 V). In the mass transport region at
165 1.75 A cm⁻² current density, a significant reduction in voltage loss of up to 136 mV was achieved
166 in LPCNGF relative to Pt₃Co/C(Um).

167 Durability represents another critical challenge for the development of ORR catalyst for fuel
168 cell. We performed accelerated stress test (AST) to investigate the stability of LPCNGF in H₂-
169 Air cell followed by testing in H₂-O₂ cell on the same MEA, using DOE's durability evaluation
170 protocol⁵. At 150 kPa_{abs} pressure in the H₂-Air cell (Fig. 4b), the performance of LPCNGF was
171 superior to that of Pt₃Co/C(Um) in terms of higher current density and peak power density (0.63
172 W cm⁻² vs. 0.45 W cm⁻²) throughout the entire voltage range. After 30,000-AST cycles, the
173 voltage loss at 0.8 A cm⁻² was negligible for LPCNGF, surpassing the target set by DOE (< 30
174 mV loss at 0.8 A cm⁻² after 30,000 AST cycles)⁵. The high peak power density was also
175 maintained, indicating that the catalyst is extremely durable. The in-situ formed graphene and the
176 well-protected PtCo alloy contribute significantly to the enhanced stability. By contrast, the
177 voltage loss at 0.8 A cm⁻² for Pt₃Co/C(Um) was 156 mV, and the peak power density showed
178 31% decay after 30,000 AST cycles. Power per gram of PGM (kW g_{PGM}⁻¹) is a valuable metric
179 for the evaluation of PGM catalyst being used in vehicles. Compared with DOE's 2025 target of
180 8 kW g_{PGM}⁻¹, the Pt power metric of LPCNGF at both beginning of life (BOL, 11.1 kW g_{Pt}⁻¹ at
181 150 kPa_{abs}, 12.2 kW g_{Pt}⁻¹ at 200 kPa_{abs}) and end of life (EOL, 10.9 kW g_{Pt}⁻¹ at 150 kPa_{abs}) after

182 30,000 cycles test in H₂-Air cell are noteworthy (Fig. 4d, right). In contrast, Pt₃Co/C(Um) failed
183 to meet DOE's target both at BOL and EOL at 150 kPa_{abs}.

184 A continued durability evaluation in H₂-O₂ cell further corroborates the excellent durability
185 and the high activity of LPCNGF. Because Pt₃Co/C(Um) was deactivated after durability
186 measurement in the H₂-Air cell, we prepared a new MEA with Pt₃Co/C(Um) at cathode as a
187 benchmark for the H₂-O₂ cell. Even having undergone 30,000 AST cycles in a H₂-Air cell, the
188 H₂-O₂ cell performance with LPCNGF at cathode still outperformed Pt₃Co/C(Um), displaying
189 larger current density and higher peak power density throughout the entire voltage range (Fig. 4c,
190 iR-corrected polarization shown in Supplementary Fig. 13). The peak power density of LPCNGF
191 reached 1.11 W cm⁻² at BOL (150 kPa_{abs}), corresponding to an effective Pt utilization of 0.044
192 g_{Pt} kW⁻¹ at cathode, which is 1.7 times that of the recently reported Pt/nitrogen modified C
193 (0.075 g_{Pt} kW⁻¹, 230 kPa_{abs})¹⁸, and rank among the highest reported in the literatures (Fig. 4f).
194 The LPCNGF delivered a MA of 2.28 A g_{Pt}⁻¹ at 0.9 V_{iR-free} at BOL (Fig. 4d, left), 2.5 times that
195 of Pt₃Co (Um) (0.92 A g_{Pt}⁻¹ at 0.9 V_{iR-free}), and 5 times of US DOE's 2025 target of 0.44 A g_{Pt}⁻¹
196 at 0.9 V_{iR-free}. After the 30,000 AST cycles, the MA of LPCNGF maintained 80% retention (1.83
197 A g_{Pt}⁻¹ at 0.9 V_{iR-free} at EOL) (Fig. 4d, left), exceeding DOE'S target which requires less than
198 40% loss of initial MA after the 30,000-cycle AST test (0.26 A g_{Pt}⁻¹ at EOL). To the best of our
199 knowledge, this is the highest MA and durability achieved ever in a PEM H₂-O₂ cell (Fig. 4e,
200 Supplementary Table 3). In comparison, Pt₃Co/C(Um) displayed significant degradation, with
201 MA loss of 45% (0.51 A g_{Pt}⁻¹ at 0.9 V_{iR-free} at EOL). Our results suggest that LPCNGF is a
202 promising candidate for widespread fuel cell use in automotive applications.

203

204 **Structure evolution and possible mechanism during ORR.** The morphology of interconnected
205 carbon nanofiber with MOF-structured beads in LPCNGF was maintained after the AST in fuel
206 cell and EDS attested to the negligible change in atomic ratios of Co:Pt:N:C (Supplementary Fig.
207 14). The average particle size and the core-shell structure of PtCo alloy were also preserved
208 (Supplementary Fig. S15). All these results suggest a durable LPCNGF structure under the harsh
209 operating conditions of a fuel cell. To better understand the origin of this extraordinary ORR
210 performance, we performed X-Ray Photoelectron Spectroscopy (XPS) and X-ray Absorption
211 Spectroscopy (XAS) to elucidate the surface composition, oxidation states, and local atomic
212 structure of LPCNGF. The Pt XPS spectrum shows a 0.2 eV positive shift in binding energy
213 after NH₃ annealing, relative to that of the material before NH₃ treatment (LPCNGF-BN, Fig.
214 5a), indicating an electron transfer between Pt and Co as a consequence of PtCo alloy formation.
215 The Co XPS result shows a re-distribution from Co⁰ dominated surface to more Co-N_x
216 terminations after NH₃ treatment (Fig. 5b). Analysis of the N 1s XPS spectrum from LPCNGF-
217 BN reveals 3 groups of N functionalization (Fig. 5c), pyridinic- (398.6 eV), pyrrolic- (400.2 eV)
218 and oxidic-N (402-405 eV)²⁴. NH₃ treatment leads to additional N incorporated into the carbon
219 matrix, and decomposition of pyrrolic-N to form additional pyridinic groups^{9,23}. As a
220 consequence, the surface is dominated with pyridinic-N. NH₃ treatment, inducing surface
221 modification by creating additional Co-N_x and pyridinic-N, would positively influence the
222 activity and electronic conductivity of the catalyst^{4,24}. Moreover, the abundant nitrogen
223 functional groups could facilitate the homogenous distribution of ionomer throughout the
224 catalyst layer, further enhancing the activity.

225 X-ray absorption near edge structure (XANES) at the Co K-edge in LPCNGF-BN includes
226 contributions from metallic Co and Co-N_x with four different features, labeled as A, B, C, and D

227 (Fig. 5d). After NH₃ treatment, features A and B were shifted to lower energy, suggesting the
228 formation of Co-Pt bonds²⁶. Feature D was blue shifted, suggesting that cobalt is positively
229 charged. Feature C increased substantially, reflecting hybridization of Co 4s and 4p orbital by Pt
230 in the alloy²⁶ and N in Co-N_x. The extended X-ray absorption fine structure (EXAFS) result at
231 Co K-edge (Supplementary Fig. 16a) further confirms the formation of Co-N_x centers, evidenced
232 from the enhanced peak intensity at 1.44 Å corresponding to Co-N bond, consistent with XPS
233 result. XANES spectrum at Pt L-III edge in LPCNGF suggests the formation of PtCo alloy as
234 evidenced by the appearance of peak at 11576 eV (Fig. 5e, red arrow). The white line (WL)
235 intensity at Pt L-III edge in LPCNGF decreased relative to that in LPCNGF-BN, indicating
236 electron transfer from Co to Pt, which tuned the Pt d-band energy leading to weakened OH_{ad}
237 binding on the Pt surface, thus improving ORR catalytic properties⁴. The formation of ordered
238 PtCo alloy is further confirmed by EXAFS (Supplementary Fig. 16b). It is worth noting that R_{Pt-Co}
239 (2.19 Å) is similar to the R_{Co-Co} (2.18 Å) (Supplementary Fig. 16a), suggesting that the
240 majority of the hetero-atomic interactions in LPCNGF are located in the Co-rich core, consistent
241 with the Pt_{thin-shell}/single-PtCo_{core} structure. The surface structure of LPCNGF catalyst is
242 schematically outlined in Fig. 5f.

243 To examine evolution of the local atomic structure or metal oxidation states in LPCNGF
244 during ORR, we collected in-situ XANES and EXAFS spectra at the Co K-edge and Pt L-edge in
245 O₂ saturated 0.1 M HClO₄ at various applied potentials (Fig. 6). When 0.8 V potential was
246 applied, XANES spectrum at Co K-edge showed that the absorption energy was slightly blue-
247 shifted compared to the dry sample (Supplementary Fig. 17a), suggesting the absorption of
248 oxygenated species (O* or OH*) on the surface Co. As the applied potential increased to 1.3 V,
249 the absorption edge at 7728 eV shifted to 7729 eV with slightly enhanced WL intensity (Fig. 6a,

250 inset), indicating charge transfer from Co to the oxygenate intermediate. EXAFS spectrum at the
251 Co K-edge at 0.8 V (Fig. 6c, Supplementary Fig. 17b) displayed appearance of Co-Co bonds at
252 2.78 Å, indicating Co atoms interconnected by di- μ -xox (μ_3 -O)(μ_2 -OH) bridges which suggests
253 the formation of edge-sharing Co octahedron²⁷. The new peak at 4.86 Å further confirms the
254 edge-sharing CoO₆ octahedron in the in-situ sample. At 1.3 V, the Co-Co bond distance
255 decreased by 0.09 Å relative to that at 0.8 V (Fig. 6c, inset), implying oxidation of Co.
256 Moreover, the peak at 1.44 Å assigned to Co-N bond shifted to 1.49 Å corresponding to Co-O
257 bond, indicating ORR takes place on Co-N site by absorbing oxygenated intermediates on to the
258 Co center.

259 WL intensity at Pt L_{III}-edge increased at elevated potential (red arrow, Fig. 6b), accompanied
260 with intensity decrease in the post-edge region (red circle). This result indicates the absorption of
261 oxygenated intermediate on the Pt surface, which increases the unoccupied d-orbitals of Pt via
262 the charge transfer from Pt to O²⁸. It is worth noting that the WL intensity at 1.3 V is still lower
263 than that of Pt foil, emphasizing the metallic state of Pt. EXAFS spectra at Pt L_{III}-edge shows
264 decreased Pt-Co peak intensity with increasing potential (Fig. 6d, inset), suggesting that the
265 surface becomes disordered during ORR. As the potential reached 1.3 V, a new weak peak at
266 1.72 Å appeared. This peak is assigned to a Pt-OH bond, which is 0.12 Å larger than the Pt-O
267 bond (1.6 Å)^{28, 29}. When the potential decreased to 0.6 V, both XANES and EXAFS spectra at
268 Co K-edge and Pt L_{III}-edge reverted to their initial state, which indicates that the chemical
269 absorption of oxygenate intermediates on the surface of Co in Co-N-GF and Pt in PtCo alloy, is a
270 reversible process during ORR. The in-situ experiments reveal that both PtCo NP and Co-N-GF
271 simultaneously contribute to the ORR activity.

272

273 **Conclusions**

274 We have presented a highly active, durable and robust LPCNGF catalyst composed of core-
275 shell structured PtCo NP dispersed over self-ORR active Co-N-GF. The Co-N-GF was
276 synthesized through electrospinning a polymer solution containing PAN and Co-MOF, followed
277 by pyrolysis at high temperature. The Co-N-GF possesses I) densely populated atomic Co-N_x
278 catalytic active sites, II) tailored high porosity, III) interconnected micro-/meso-/macro-pores, V)
279 N-doped graphene. Such a unique hierarchical porous structure, on one hand, enhances Pt mass
280 activity by improving Pt accessibility to the reactant; on the other hand, facilitates an excellent
281 water management capability. The abundant nitrogen functionalities enable the uniform
282 distribution of ionomer throughout the electrode layer, which further enhances the Pt activity.
283 Moreover, Co-N-GF is self-ORR highly active. Therefore, with a total Pt loading (anode +
284 cathode) of 0.091 mg cm⁻², MEA assembled with LPCNGF as cathode catalyst delivered the
285 highest mass activity of 2.28 A g_{Pt}⁻¹ at 0.9 V_{iR-free} in PEM H₂-O₂ cell, 438 mA cm⁻² current
286 density at 0.8 V in PEM H₂-Air cell, and exhibited excellent durability with 80% MA retention
287 after a 30,000-cycle AST in H₂-Air cell and a continued 30,000-cycle AST in H₂-O₂ cell,
288 surpassing US DOE's 2025 target for ORR catalyst under PEMFC conditions. The MEA
289 displayed an effective Pt utilization of 0.044 g_{Pt} kW⁻¹ in H₂-O₂ cell, and 11.1 kW g_{PGM}⁻¹ at 150
290 kPa_{abs} in H₂-Air cell. These performance metrics enable a fuel cell powered vehicle to be
291 competitive with ICE autos. The in-situ formed N-doped graphene, benefiting from the
292 combination of Co-MOF and PAN fiber, contributes to the significantly improved durability, and
293 electron conductivity of LPCNGF. Furthermore, insights obtained from in-situ XANES and
294 EXAFS experiments reveal that a) oxygenated species are formed in-situ over the surface of Co-
295 N-GF during ORR; b) Co-N-GF catalyst and PtCo contribute to the ORR simultaneously; c) the

296 structure evolution of both Co-N-GF and PtCo alloy are reversible during ORR. We believe that
297 the unprecedented activity and durability of LPCNGF will boost widespread commercialization
298 of fuel cells in automobile applications, which will help to reduce reliance on fossil fuels.

299

300 **Methods**

301 **Synthesis of Co-MOF:** Preparation of Co-MOF was based on the existing literature¹⁵. Specifically, 1 g
302 Co(NO₃)₂.6H₂O was dissolved in 80 ml of methanol, sonicated for 10 min and labeled as solution A. 2.25 g mIm
303 was dissolved in 100 ml of methanol, sonicated for 10 min and labeled as solution B. Solution A mixed with B
304 dropwise, followed by stirring for 10 min at room temperature to produce a heterogeneous violet mixture, which was
305 then sealed and kept at R.T for 12 h. The violet crystal was collected by centrifugation with a rotation rate of 6000
306 rpm, and then dried at 60 °C under vacuum overnight.

307

308 **Fabrication of Co-MOF/PAN fiber:** PAN was dissolved in DMF at concentration of 150 mg ml⁻¹. The mixture
309 was stirred at 40 °C overnight. Co-MOF was dissolved into DMF at concentration of 100 mg ml⁻¹, and ball milled at
310 400 rpm for 3 h in a planetary ball mill. Taking 36% Co-MOF in Co-MOF/PAN fiber as a representative
311 composition, PAN solution and Co-MOF solution were mixed with volume ratio of 2:3 followed by ball milling at
312 400 rpm for 1 h to prepare the final slurry. This slurry was transferred to 2 ml syringe and then fabricated into Co-
313 MOF/PAN nanofiber using the electrospinning conditions – 10 kV, feed rate of 0.003 ml min⁻¹ and a spinneret-to-
314 collector distance of 10 cm.

315

316 **Co-N-GF catalyst synthesis:** The Co-MOF/PAN nanofiber was converted to Co-N-GF nanofiber by pyrolysis first
317 at 750 °C for 6 h, and then at 1000 °C for 1.5 h under flowing Ar, with a heating ramp rate of 3 °C min⁻¹. After
318 pyrolysis, the carbon nanofiber was soaked in 0.5 M H₂SO₄ at R.T for 2 h to leach out the inactive Co metal,
319 followed by stirring in DI water overnight and drying at 80 °C under vacuum. The obtained nanofiber was denoted
320 as Co-N-GF. The cobalt content in Co-N-GF was ~ 8 wt.%.

321

322 **LPCNGF catalyst synthesis:** 5.1 mg trimethyl(methylcyclopentadienyl)platinum(IV) was dissolved in oleylamine,
323 and sonicated for 1 min to form a transparent solution, followed by rapid addition of 60 mg Co-N-GF . The mixture
324 was sonicated for 9 min to form a homogenous slurry, which was then sealed under air and heated at 196 °C in an oil
325 bath for 1 h. The resulting sample was collected by centrifuging, and followed by drying at 60 °C under vacuum.
326 The obtained porous powder was finally heat-treated under flowing ammonia at 750 °C for 30 min. The catalyst thus
327 obtained was named as LPCNGF. The overall Pt loading in the sample was quantified by EDS.

328

329 **Electrochemical measurement:** The electrochemical performance was first evaluated in O₂ saturated 0.1 M HClO₄
330 electrolyte at room temperature using CHI electrochemical station (Model 760C) in a conventional three-electrode
331 electrochemical cell with mercury/mercury sulfate as reference electrode and gold wire as counter electrode. The ink
332 was prepared by mixing 1 mg of catalyst powder with 600 μl of mixture solution of 5 % Nafion and methanol. After
333 2 h of sonication, 10 μl of ink was applied onto a glass carbon electrode (0.2472 cm²) representing the working
334 electrode. The Pt loading of the electrode was ~ 4.0 μg_{Pt}·cm⁻² for LPCNGF. An initial conditioning step of ~ 20
335 cyclic voltammogram (CV) cycles between 0 V and 1.2 V vs. RHE was applied. Afterward, ORR activity was
336 recorded using linear sweep voltammetry (LSV) in a range from 0 V to 1.2 V versus reversible hydrogen electrode
337 (RHE) at a scan rate of 10 mV s⁻¹ and rotation rate of 1600 rpm in oxygen saturated 0.1 M HClO₄ electrolyte.
338 Catalyst stability was studied by CV between 0.4 V and 1.0 V with 10,000 cycles at a scan rate of 50 mV s⁻¹.
339 Electrochemical surface area was determined by integrating hydrogen adsorption charge on CV curve after double-
340 layer correction and assuming a value of 210 μC cm⁻² for the absorption of a hydrogen monolayer. For comparison,
341 commercial 30 wt.% Pt₃Co obtained from Umicore company was studied as benchmark catalyst using the same ink
342 deposition technique and testing protocol. The Pt loading of the electrode was ~ 80 μg_{Pt}·cm⁻² and ~ 14 μg_{Pt}·cm⁻² for
343 Pt/C and Pt₃Co/C(Um), respectively. The number of transferred electrons n, the percentage of yield H₂O₂, and Pt
344 mass activity were derived from the following equations:

345

346
$$n = \frac{4I_d}{I_d + \frac{I_r}{N}}$$

347 (1)

348

349

350

$$H_2O_2(\%) = 200 \times \frac{\frac{I_r}{N}}{\frac{I_r}{N} + I_d} \quad (2)$$

353

354

$$I_m = \frac{-I_k}{m_{Pt}} \quad (3)$$

356

357 Where I_k is the kinetic current, m_{Pt} is the Pt mass in the catalyst deposited on the disk, I_d is the disk current, I_r is the
 358 ring current and N is the ring collection efficiency (37 %).

359

360 **MEA preparation and fuel cell test:** The catalyst ink was prepared by ultra-sonicating the mixture of catalyst
 361 powder and Nafion ionomer solution diluted by isopropanol/DI water for 2 h. The weight ratios of ionomer to
 362 carbon were ~ 0.76 – 0.86 for cathode and 0.6 for anode. The “ink” was applied directly to Nafion 211 membrane
 363 (DuPont) with active area of 5 cm² through air brush painting, which was then sandwiched between two gas
 364 diffusion layers (Sigracet 25BC) to assemble the final MEA. The performance testing was conducted in a fuel cell
 365 test station (Scribner 850e). Polarization curves were recorded at various temperatures (60, 70, 80, 90 °C), relative
 366 humidity (RH) levels (50, 75, 100%) and absolute pressures (100, 150, 230 kPa_{abs}). For H₂-O₂ cell, the flow-rate was
 367 fixed at 200 ml min⁻¹ for both H₂ and O₂. For H₂-Air cell test, the flowrate for H₂ was maintained at 200 ml min⁻¹,
 368 while different flow-rates (200, 520, 580, 780, 1000 ml min⁻¹) were applied for air. The accelerated stress test (AST)
 369 was conducted by square wave voltage cycling at 0.6 V for 3 s and 0.95 V for 3 s with 200 ml min⁻¹ H₂ feeding into
 370 the anode and 75 ml min⁻¹ N₂ feeding into the cathode based on DOE’s AST protocol required for MEA durability
 371 evaluation⁵; the cell was set at 80 °C and 100 % RH and the back pressures of both cathode and anode were set at
 372 ambient (101 KPa). After completion of the voltage cycles, a voltage recovery (VR) process was performed: the cell
 373 was held at 0.1 V under H₂-Air for 1 h at 40 °C, 150 % RH, and 150 kPa_{abs}, followed by application of various
 374 voltages between 0.1 V and 0.85 V for different time periods³⁰. Current-voltage polarization was then recorded to
 375 measure changes in catalyst activity and durability. The H₂-Air cell and H₂-O₂ cell durability tests were performed
 376 on the same MEA for our LPCNGF catalyst. For Pt mass activity evaluation, the H₂-O₂ cell was held at 0.9 V for 15
 377 min, and the Pt mass activity was recorded by averaging the last minute value after applying hydrogen cross-over

378 correction and a short VR process for cathode at 0.9 V with flowing N₂ for 5 min. Each durability evaluation of
379 LPCNGF was conducted 3 times to ensure reproducibility. EIS was recorded at various voltages of 0.9 V, 0.8 V, 0.7
380 V, 0.6 V, 0.5 V, 0.4 V for both H₂-O₂ cell and H₂-Air cell at 1000 Hz. Prior to the experiments, a “break-in” step
381 was applied³⁰: first, the cells were heated to 80 °C and held at open circuit voltage (OCV) in H₂-Air. After this step, a
382 series of voltage cycles between 0.6 and 0.9 V with different RH were conducted.

383

384 **Characterization:** The catalyst structure was probed using a Bruker diffractometer D8 Advance with Cu K α
385 radiation (characteristic wavelength $\lambda = 1.54051 \text{ \AA}$). XPS data was acquired using a PHI 5000 VersaProbe II system
386 (Physical Electronics) that is attached to an argon-atmosphere glovebox to avoid any contamination of moisture and
387 air. The X-ray source was monochromatic Al K α radiation ($h\nu = 1486.6 \text{ eV}$) which was set at Ar+ -ion and electron
388 beam sample neutralization, fixed analyzer transmission mode. The spot size for X-ray beam was set to 100 μm . The
389 spectra of all samples were collected at pass energy of 23.50 eV and electron escape angle of 45° to the sample
390 plane. The catalyst morphologies and elemental compositions were characterized by high-resolution transmission
391 electron microscopy (HR-TEM) and Electron energy-loss spectroscopy (EELS) using Argonne’s Chromatic
392 Aberration-Corrected TEM (ACAT) operated at 80 KV. High-angle annular dark-field scanning transmission
393 electron microscopy (HAADF-STEM) images and energy-dispersive X-ray spectroscopy (EDS) were taken on a FEI
394 Talos operating at 200 KV. Scanning electron microscopy (SEM) images were acquired with a Quanta 400F ESEM
395 microscope. The specific surface area and the micro/meso/macro-porosity of the catalyst were evaluated by the
396 Brunauer-Emmett-Teller (BET) method at liquid nitrogen temperature in a Micromeritics ASAP2020 surface area
397 analyzer. The degree of graphitization of the Co-N-G nanofiber was determined with an Invia Renishaw 2000
398 microscope spectrometer with an Ar Ne laser at 633 nm wavelength.

399

400 **XAS measurement:** XAS measurements, including XANES and EXAFS, were conducted under ambient
401 temperature at Beamline 12 BM of the Advanced Photon Source at Argonne National Laboratory. The XAS
402 measurements were performed in fluorescence-transmission mode, where the data collected from LPCNGF were in
403 fluorescence mode and data collected from references placed behind the sample were in transmission mode. XAS
404 spectra were collected at Pt L_{III} edge and Co K-edge, respectively. For ex-situ measurements, samples were packed
405 as fine powder with optical thickness equivalent of e^{-1} total X-ray absorption. For in-situ measurements, samples

406 were analyzed in a home-made in-situ cell, where O₂ saturated 0.1 M HClO₄ was used as electrolyte, and
407 Hg/Hg(SO₄)₂ and gold wire were used as reference and counter electrode, respectively. A graphene sheet with 0.1
408 mg cm⁻² of catalyst loading was used as the working electrode. After activation from 0.05 V to 1 V to achieve a
409 stable state, XAS measurements were performed at elevated voltage of 0.8 V, 1.1 V, 1.3 V, and then decreased to
410 1.2 V and 0.6 V (re-reduction). At each potential, the catalyst was allowed to stabilize for 10 min before XAS
411 measurement. The applied potential was held for 1 h for data collection at each point. XAS data processing was
412 performed using ATHENA and ARTEMIS. EXAFS data were fit to a K window of 3 ~ 12 Å⁻¹ with single scattering
413 pathways. All spectra were calibrated, aligned, normalized and back-ground-subtracted per ATHENA data analysis
414 protocols.

415

416 **Data availability**

417 The data that support the findings of this study are available within the paper and its Supplementary Information or
418 from the corresponding author upon reasonable request

419

420 **References**

- 421 1. Gasteiger H. A., Kocha S. S., Sompalli B., Wagner F. T., Activity benchmarks and requirements for Pt, Pt-
422 alloy, and non-Pt oxygen reduction catalysts for PEMFCs. *Appl. Catal. B* **56**, 9-35 (2005).
- 423 2. Wagner F. T., Lakshmanan B., Mathias M. F., Electrochemistry and the future of the automobile. *Phys.
424 Chem. Lett.* **1**, 2204-2219 (2010).
- 425 3. Debe M. K., Electrocatalyst approaches and challenges for automotive fuel cells. *Nature* **486**, 43-51 (2012).
- 426 4. Chong L., *et al.* Ultralow-loading platinum-cobalt fuel cell catalysts derived from imidazolate frameworks.
427 *Science* **362**, 1276-1281(2018).
- 428 5. DOE FCTTR, US DRIVE Partnership. Fuel Cell Technical Team Roadmap, November 2017,
429 https://www.energy.gov/sites/prod/files/2017/11/f46/FCTT_Roadmap_Nov_2017_FINAL.pdf.
- 430 6. Steele B. C. H., Heinzel A., Materials for fuel-cell technologies. *Nature* **414**, 345 (2001).
- 431 7. Park Y. -C., Tokiwa H., Kakinuma K., Watanabe M., Uchida M., Effects of carbon supports on Pt
432 distribution, ionomer coverage and cathode performance for polymer electrolyte fuel cells. *J. Power
433 Sources* **315**, 179-191 (2016).

- 434 8. Yarlagadda V, et al. Boosting Fuel Cell Performance with Accessible Carbon Mesopores. *ACS Energy*
435 *Letters* **3**, 618-621 (2018).
- 436 9. Du L, Prabhakaran V, Xie X, Park S, Wang Y, Shao Y. Low-PGM and PGM-Free Catalysts for Proton
437 Exchange Membrane Fuel Cells: Stability Challenges and Material Solutions. *Adv. Mater.* 1908232 (2020).
- 438 10. Kodama K, Nagai T, Kuwaki A, Jinnouchi R, Morimoto Y. Challenges in applying highly active Pt-based
439 nanostructured catalysts for oxygen reduction reactions to fuel cell vehicles. *Nat. Nanotechnol.* **16**, 140-147
440 (2021).
- 441 11. Jaouen Fdr., Lefe`vre M., Dodelet J.-P., Cai M., Heat-treated Fe/N/C catalysts for O₂ electroreduction: Are
442 active sites hosted in micropores? *J. Phys. Chem. B* **110**, 5553-5558 (2006).
- 443 12. Shui J., Chen C., Grabstanowicz L., Zhao D., Liu D.J., Highly efficient nonprecious metal catalyst prepared
444 with metal-organic framework in a continuous carbon nanofibrous network. *PNAS USA* **112**, 10629-10634
445 (2015).
- 446 13. Chung H.T., et al. Direct atomic-level insight into the active sites of a high-performance PGM-free ORR
447 catalyst. *Science* **357**, 479-484 (2017).
- 448 14. Sun T., et al. Single-atomic cobalt sites embedded in hierarchically ordered porous nitrogen-doped carbon
449 as a superior bifunctional electrocatalyst. *PNAS* **115**, 12692–12697 (2018).
- 450 15. Chong L., et al. Investigation of Oxygen Reduction Activity of Catalysts Derived from Co and Co/Zn
451 Methyl-Imidazolate Frameworks in Proton Exchange Membrane Fuel Cells. *ChemElectroChem* **3**, 1541-
452 1545 (2016).
- 453 16. Wang L., et al. Tunable intrinsic strain in two-dimensional transition metal electrocatalysts. *Science* **363**,
454 870-874 (2019).
- 455 17. Zhou Z., Liu T., Khan A. U., Liu G., Block copolymer-based porous carbon fibers. *Sci. Adv.* **5**, 6852
456 (2019).
- 457 18. Ott S., et al. Ionomer distribution control in porous carbon-supported catalyst layers for high-power and
458 low Pt-loaded proton exchange membrane fuel cells. *Nat. Mater.* **19**, 77-85 (2020).
- 459 19. Wang X., et al. N-Doping of Graphene Through Electrothermal Reactions with Ammonia. *Science* **324**,
460 768-771 (2009).

- 461 20. Lefèvre M., Proietti E., Jaouen F., Dodelet J.-P., Iron-Based Catalysts with Improved Oxygen Reduction
462 Activity in Polymer Electrolyte Fuel Cells. *Science* **324**, 71-74 (2009).
- 463 21. Sun L-X, Okada T. Studies on interactions between Nafion and organic vapours by quartz crystal
464 microbalance. *J. Membr. Sci.* **183**, 213-221 (2001).
- 465 22. Barron A. R., Characterization of Graphene by Raman Spectroscopy. *Physical Methods in Chemistry and*
466 *Nano Science* (2015).
- 467 23. Zitolo A., *et al.* Identification of catalytic sites in cobalt-nitrogen-carbon materials for the oxygen reduction
468 reaction. *Nat. Commun.* **8**, 957 (2017).
- 469 24. Guo D, Shibuya R, Akiba C, Saji S, Kondo T, Nakamura J. Active sites of nitrogen-doped carbon materials
470 for oxygen reduction reaction clarified using model catalysts. *Science* **351**, 361-365 (2016).
- 471 25. Arrigo R., Hävecker M., Schlögl R., Su D. S., Dynamic surface rearrangement and thermal stability of
472 nitrogen functional groups on carbon nanotubes. *Chem. Comm.* **40**, 4891-4893 (2008).
- 473 26. Hlil E. K., BaudoingSavois R., Moraweck B., Renouprez A. J., X-ray Absorption Edges in Platinum-Based
474 Alloys. 2. Influence of Ordering and of the Nature of the Second Metal. *J. Phys. Chem. Lett.* **100**, 3102-
475 3107 (1996).
- 476 27. Risch M, Khare V, Zaharieva I, Gerencser L, Chernev P, Dau H. Cobalt-Oxo Core of a Water-Oxidizing
477 Catalyst Film. *J. Am. Chem. Soc.* **131**, 6936-6937 (2009).
- 478 28. Conway B. E., Electrochemical oxide film formation at noble metals as a surface-chemical process. *Prog.*
479 *Surf. Sci.* **49**, 331–345 (1995).
- 480 29. Poverenov E., *et al.* Evidence for a terminal Pt(iv)-oxo complex exhibiting diverse reactivity. *Nature* **455**,
481 1093-1096 (2008).
- 482 30. Kabir S, et al. Elucidating the Dynamic Nature of Fuel Cell Electrodes as a Function of Conditioning: An ex
483 Situ Material Characterization and in Situ Electrochemical Diagnostic Study. *ACS Appl. Mater. Interfaces*
484 **11**, 45016-45030 (2019).
- 485 31. Li J., *et al.* Hard-Magnet L10-CoPt Nanoparticles Advance Fuel Cell Catalysis. *Joule* **3**, 124-135 (2019).
- 486 32. Han B., *et al.* Record activity and stability of dealloyed bimetallic catalysts for proton exchange membrane
487 fuel cells. *Energy. Environ. Sci.* **8**, 258-266 (2015).

488 33 . Steinbach A., Annual Merit Review DOE Hydrogen and Fuel Cells and Vehicle Technologies Programs,
489 Washington, DC, 2014, http://www.hydrogen.energy.gov/pdfs/review14/fc104_steinbach_2014_o.pdf.
490 34. Popov B. N., Annual Merit Review DOE Hydrogen and Fuel Cells and Vehicle Technologies Programs,
491 Washington, DC, 2014, http://www.hydrogen.energy.gov/pdfs/review14/fc088_popov_2014_o.pdf.
492 35. Kongkanand A., Annual Merit Review DOE Hydrogen and Fuel Cells and Vehicle Technologies Programs,
493 Washington, DC, 2018, https://www.hydrogen.energy.gov/pdfs/review18/fc144_kongkanand_2018_o.pdf.
494 36. Jung W. S., Popov B. N., New method to synthesize highly active and durable chemically ordered fct-PtCo
495 cathode catalyst for PEMFCs. *ACS Appl. Mater. Interfaces* **9**, 23679-23686 (2017).

496 Acknowledgements

497 LC is grateful for support through the Maria Goeppert Mayer Fellowship at Argonne National Laboratory. We
498 acknowledge use of Argonne National Laboratory's Advanced Photo Source, U.S. DOE Office of Science User
499 Facilities, supported by the U.S. DOE Office of Science, under contract DE-AC02-06CH11357. This work was
500 performed, in part, at the Center for Nanoscale Materials, a U.S. Department of Energy Office of Science User
501 Facility, and supported by the U.S. Department of Energy, Office of Science, under Contract No. DE-AC02-
502 06CH11357.

503

504 Author contributions

505 L.C designed research; L.C, Z.Y, performed research; J.G, Y.L conduced TEM; L.C, Z.Y, D.A analyzed data; and
506 L.C, I.B and D.A wrote the paper. All the authors discussed and commented on the manuscript.

507

508 Competing Interests

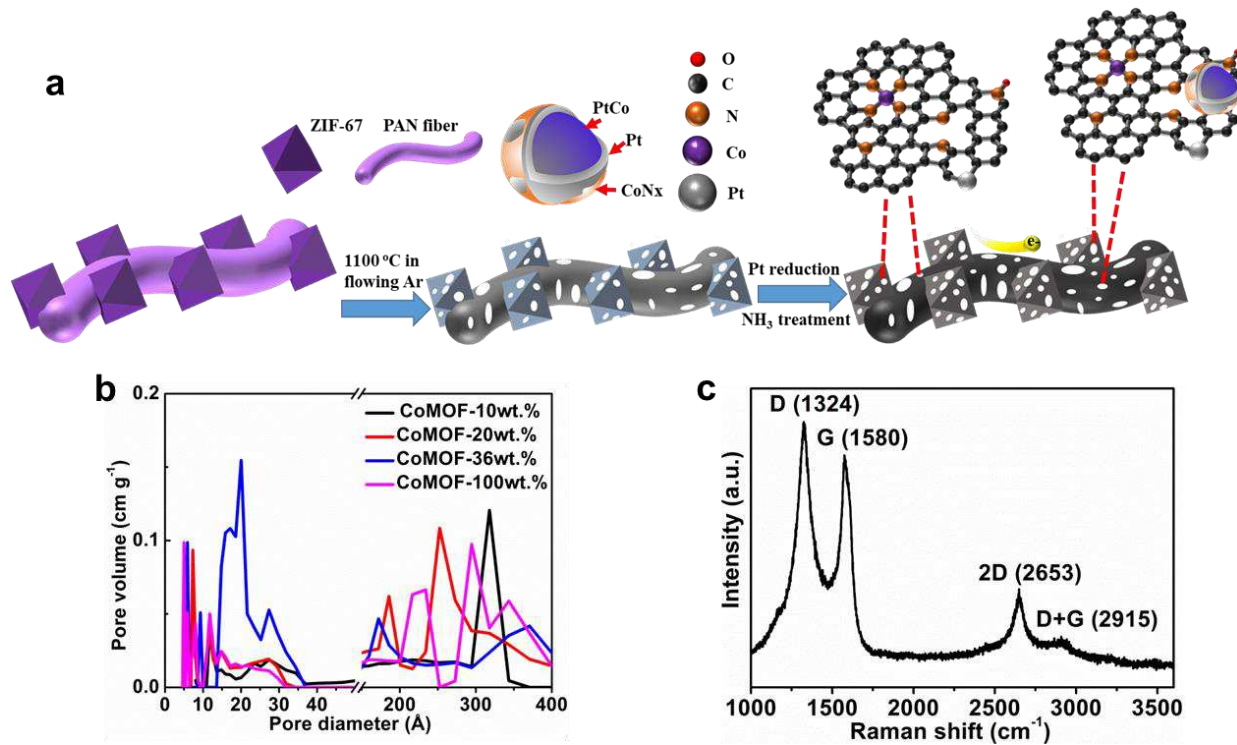
509 The authors declare no conflict of interest.

510

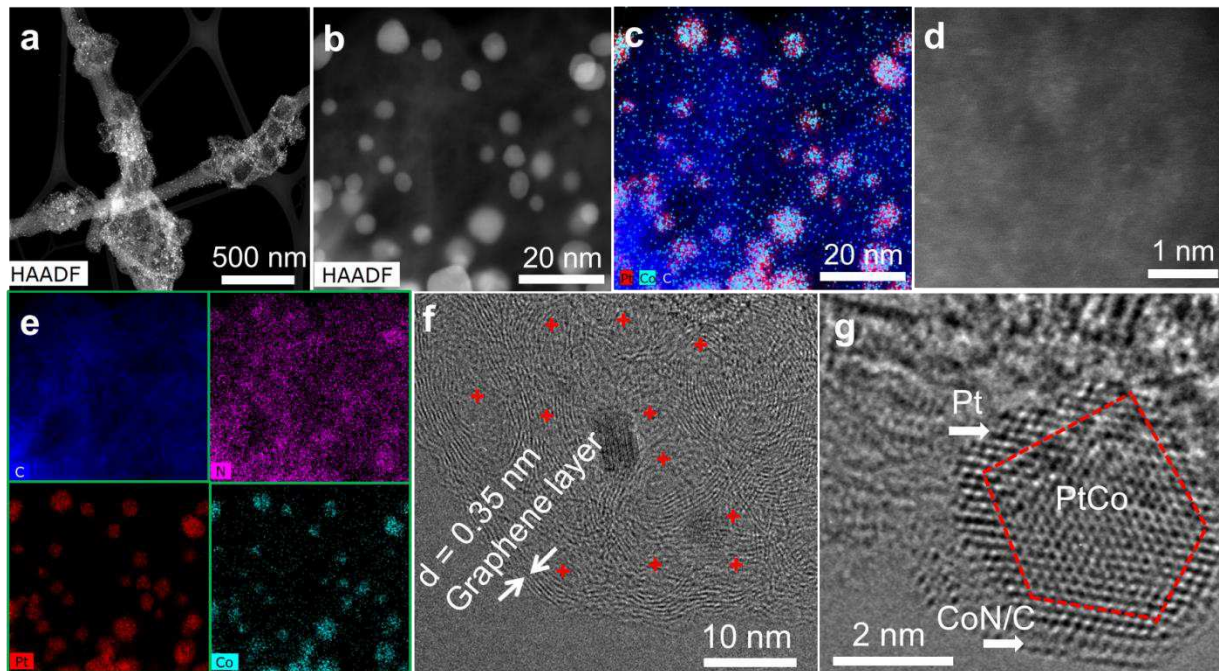
511 Additional information

512 Supplementary information is available

513 Correspondence and requests for materials should be addressed to L.C, J.G, or D.A



516 **Fig. 1 Overview of synthesis approach and structure characterization.** **a** Schematic illustration for the synthesis
 517 of LPCNGF with ammonolysis in pure NH₃ to form additional PGM-free active sites including Co-Nx, Pyridinic-N,
 518 and micropore, PtCo alloys, as well as CoN/C protecting layer for PtCo alloys. **b** BET micropore-mesopore size
 519 distribution for different Co-N-GF samples as function of Co-MOF content in the CoMOF/PAN fiber precursors. **c**
 520 Raman spectrum of LPCNGF, evidencing the graphene-nature of the formed carbon by introducing PAN fiber.

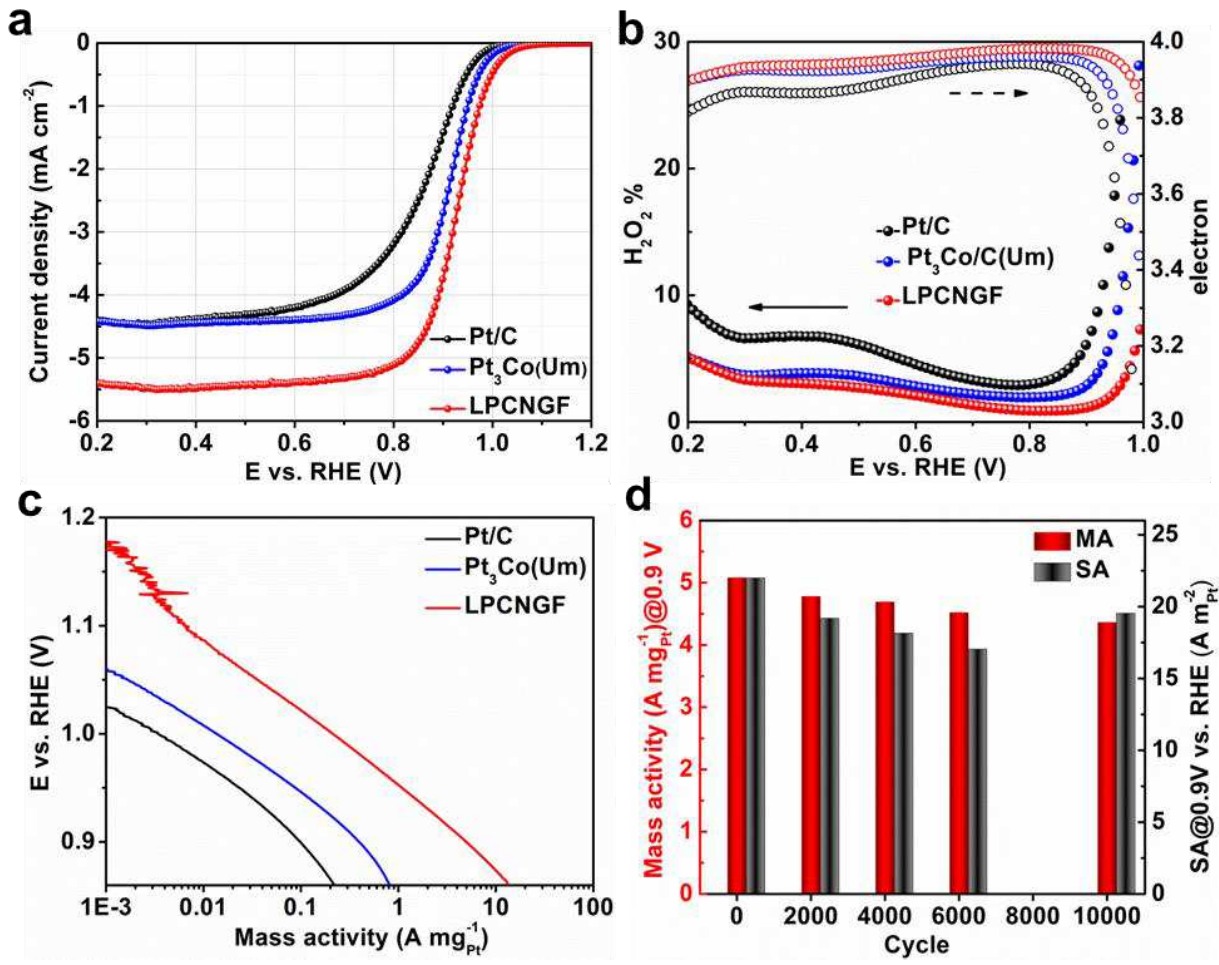


522

523

524 **Fig. 2 Morphology characterization of LPCNGF.** **a** HAADF-STEM image of two single fibers. **b** HAADF-
 525 STEM image of Pt-Co alloy NPs in LPCNGF. **c, e** the corresponding EDS elemental mapping. **d** Atomic-resolution
 526 HAADF-STEM image of isolated single Co atoms distributed across the carbon surface. **f** HRTEM image of carbon
 527 from “beads”, showing curved thin graphene layer. **g** HRTEM image of a representative Pt-Co alloy NP with
 528 ordered PtCo core and Pt shell partially covered by CoN/C terraces.

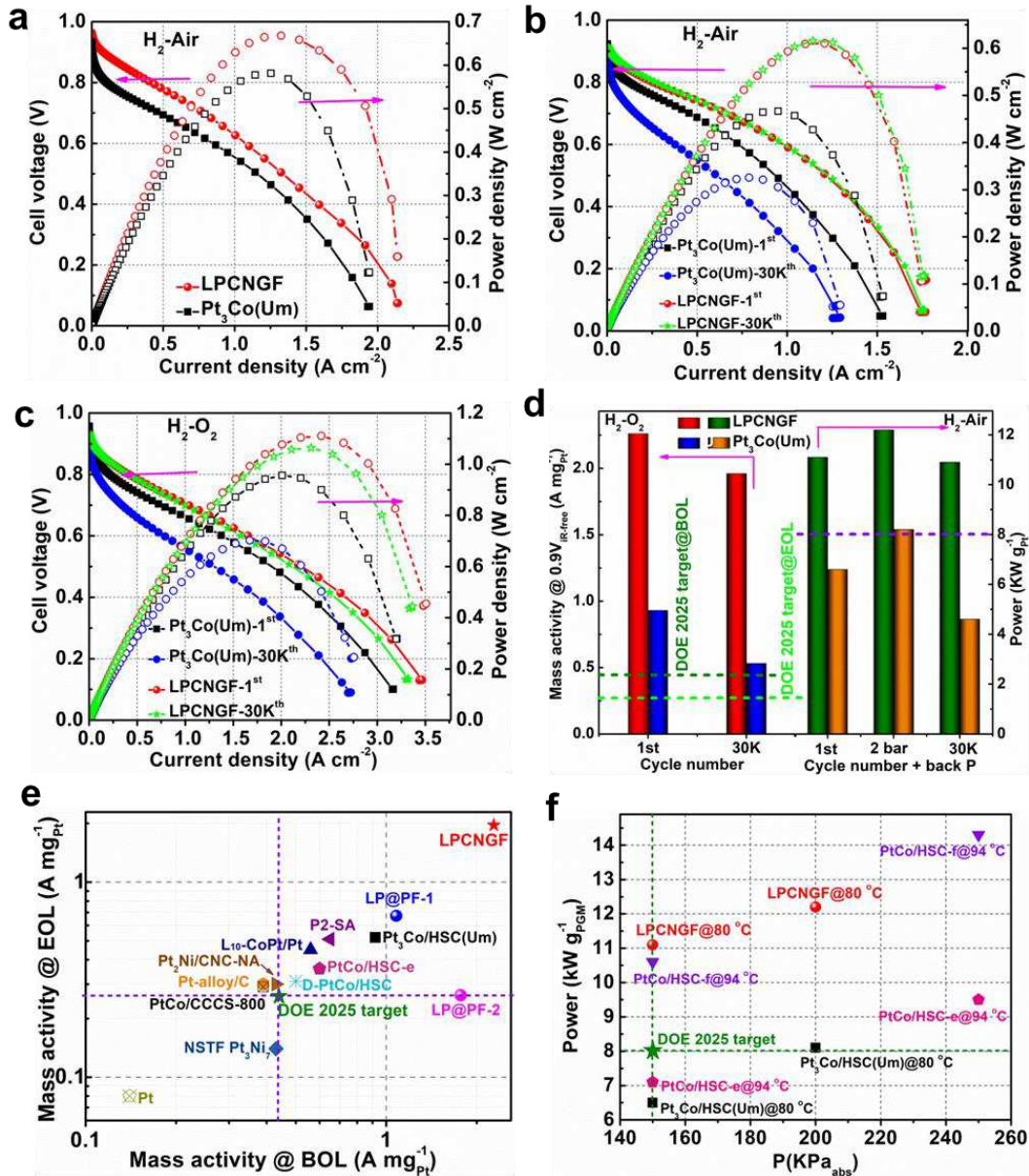
529



530

531 **Fig. 3** Electrochemical performance evaluation of LPCNGF by the RRDE method. **a** Steady-state ORR
 532 polarization plot of LPCNGF catalyst recorded at a scan rate of 10 mV s^{-1} and 1600 r.p.m in O_2 saturated 0.1 M
 533 HClO_4 electrolyte, and compared with that of 20 wt.% Pt/C and 30 wt.% $\text{Pt}_3\text{Co}/\text{C}(\text{Um})$. Pt loading is $\sim 4 \mu\text{g}_{\text{Pt}} \text{ cm}^{-2}$
 534 for LPCNGF, $\sim 80 \mu\text{g}_{\text{Pt}} \text{ cm}^{-2}$ for Pt/C and $\sim 14 \mu\text{g}_{\text{Pt}} \text{ cm}^{-2}$ for $\text{Pt}_3\text{Co}/\text{C}(\text{Um})$. **b** The corresponding H_2O_2 yield and
 535 electron transfer number. **c** The corresponding MA Tafel plots. **d** MA and SA as function of cycle number by RRDE.

536

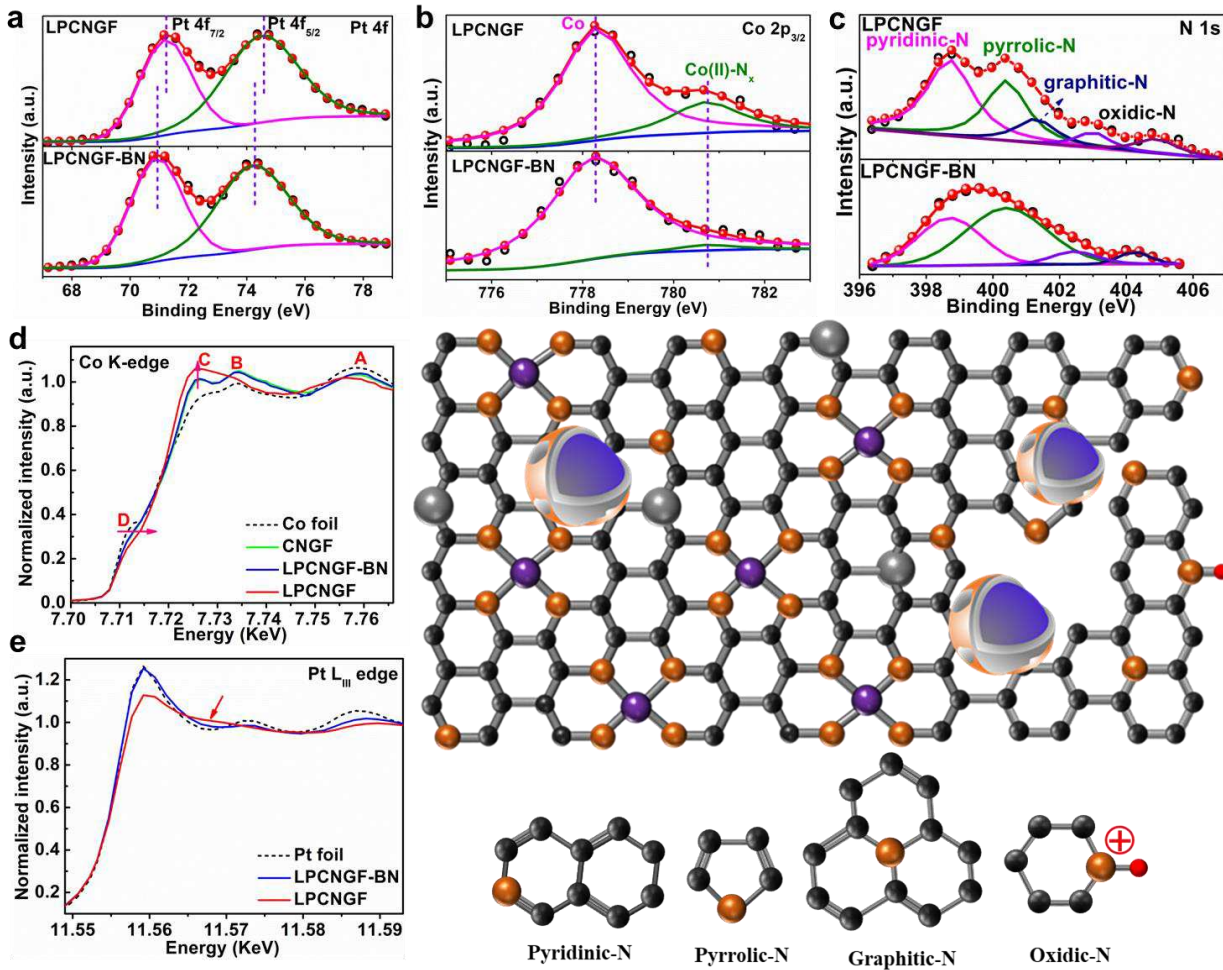


537

538

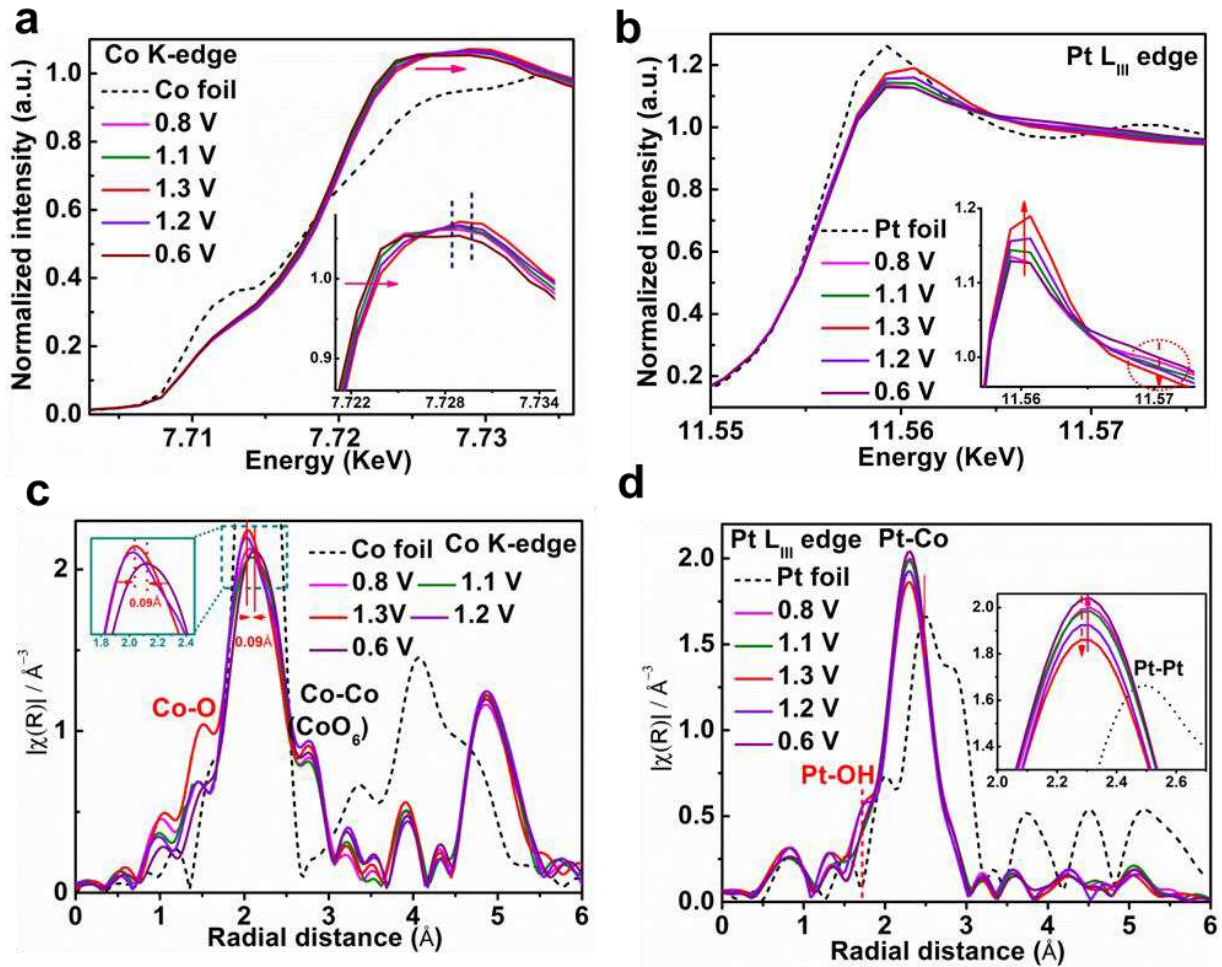
539 **Fig. 4 PEMFC performance and durability evaluation of LPCNGF.** **a** H₂-Air fuel cell polarization and power
 540 density plots of LPCNGF under Pa=Pc=200 kPa_{abs}. MEA with 30 wt.% Pt₃Co(Um) as cathodic catalyst was tested
 541 under the same condition as benchmark. **b** H₂-Air fuel cell i-v polarization and power density before and after 30
 542 000 cycles AST test under Pa=Pc=150 kPa_{abs}. **c** i-v polarization and power density for the same MEA with LPCNGF
 543 catalyst in a continued 30 000 AST test in a H₂-O₂ fuel cell after test in (**b**). **d** fuel cell MA at 0.9 V_{iR-free} and power
 544 per gram of Pt before and after 30 000 AST. **e** MAs of different catalysts at 0.9 V_{iR-free} before and after 30 000 AST
 545 in PEMFC. Catalysts include those from this work and previous reported ones: LP@PF-1/2⁴, L10-CoPt/Pt³¹, P2-

546 SA³², NSTF Pt₃Ni₇³³, Pt2Ni/CNC-NA³⁴, PtCo/HSC-e³⁵, Pt-alloy/C and Pt³, PtCo/CCCS-800³⁶. **f** power per gram
547 PGM of catalysts from this work and the previous reported³⁵. For all the fuel cell tests, membrane = Nafion 211,
548 temperature = 80 °C, cathode loading ≤ 0.056 mg_{Pt} cm⁻², anode loading ≤ 0.035 mg_{Pt} cm⁻², RH_a = RH_c = 100 %. For
549 H₂-Air cell, P_{H2} = P_{Air} = 150 kPa_{abs} or 200 kPa_{abs}; H₂ flow rate = 200 ml min⁻¹, and air flow rate = 780 ml min⁻¹; for
550 H₂-O₂ cell, P_{H2} = P_{O2} = 150 kPa_{abs}, H₂ flow rate = O₂ flow rate = 200 ml min⁻¹.



551

552 **Fig. 5 Structural characterization of the LPCNGF catalyst.** XPS spectra of **a** Pt 4f, **b** Co 2p_{3/2} and **c** N 1s
 553 binding energy before (-BN) and after NH₃ treatment. XANES spectra at **d** Co K-edge and **e** Pt L_{III}-edge before and
 554 after NH₃ treatment with the metal foil as reference. **f**, Schematic illustration of LPCNGF structure.



555

556 **Fig. 6** In-situ X-ray absorption spectra of LPCNGF. **a** Co K-edge and **b** Pt L_{III}-edge XANES spectra measured at
 557 different potentials ascending from 0.8 V, 1.1 V to 1.3 V and then descending to 1.2 V and 0.6 V in O₂ saturated 0.1
 558 M HClO₄ electrolyte. Insets magnify the WL region, clearly showing structure evolution during the ORR process.
 559 FT EXAFS spectra at **c** Co K-edge and **d** Pt L_{III}-edge collected at potentials ascending from 0.8 V, 1.1 V to 1.3 V
 560 and then descending to 1.2 V and 0.6 V in O₂ saturated 0.1 M HClO₄ electrolyte. Insets are enlargements of **c** Co-Co
 561 and **d** Pt-Co peaks.

Figures

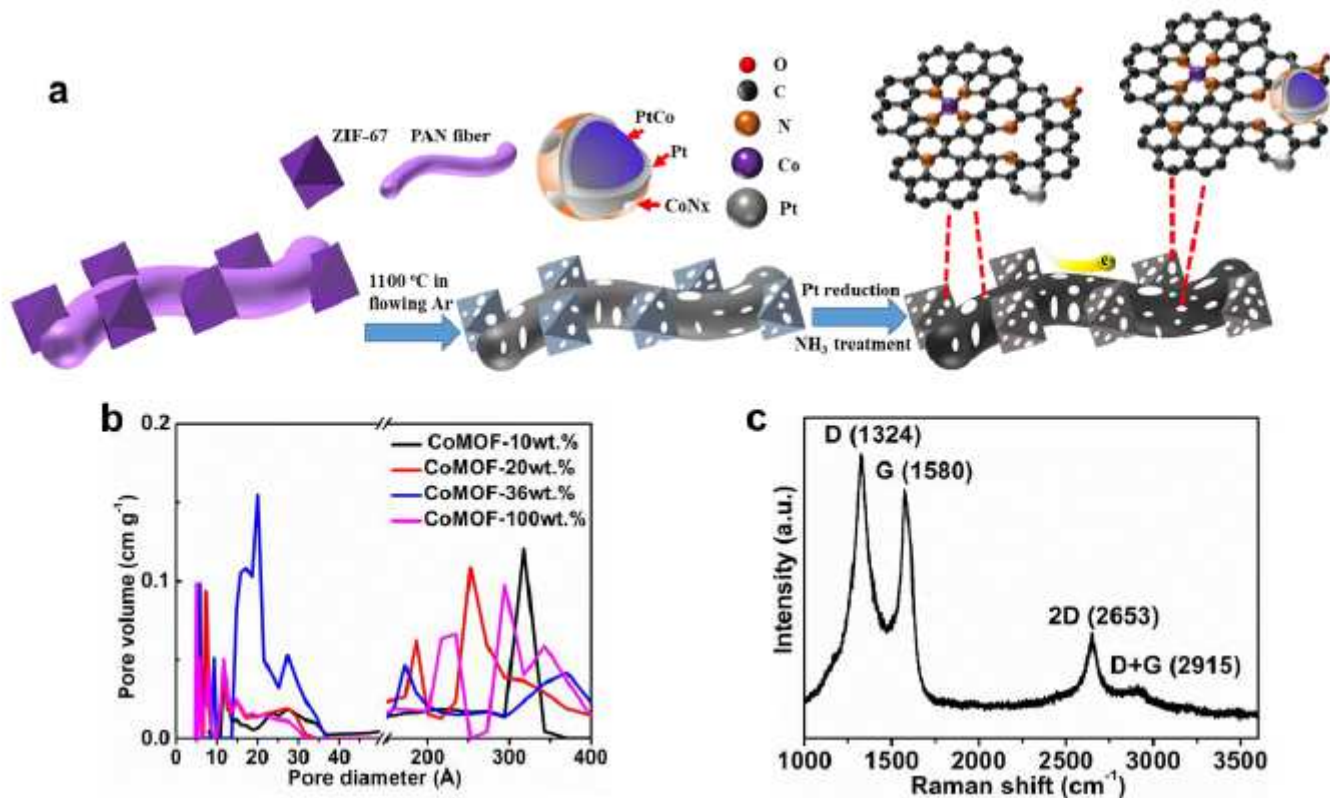


Figure 1

Overview of synthesis approach and structure characterization. a Schematic illustration for the synthesis of LPCNGF with ammonolysis in pure NH₃ to form additional PGM-free active sites including Co-Nx, Pyridinic-N, and micropore, PtCo alloys, as well as CoN/C protecting layer for PtCo alloys. b BET micropore-mesopore size distribution for different Co-N-GF samples as function of Co-MOF content in the CoMOF/PAN fiber precursors. c Raman spectrum of LPCNGF, evidencing the graphene-nature of the formed carbon by introducing PAN fiber.

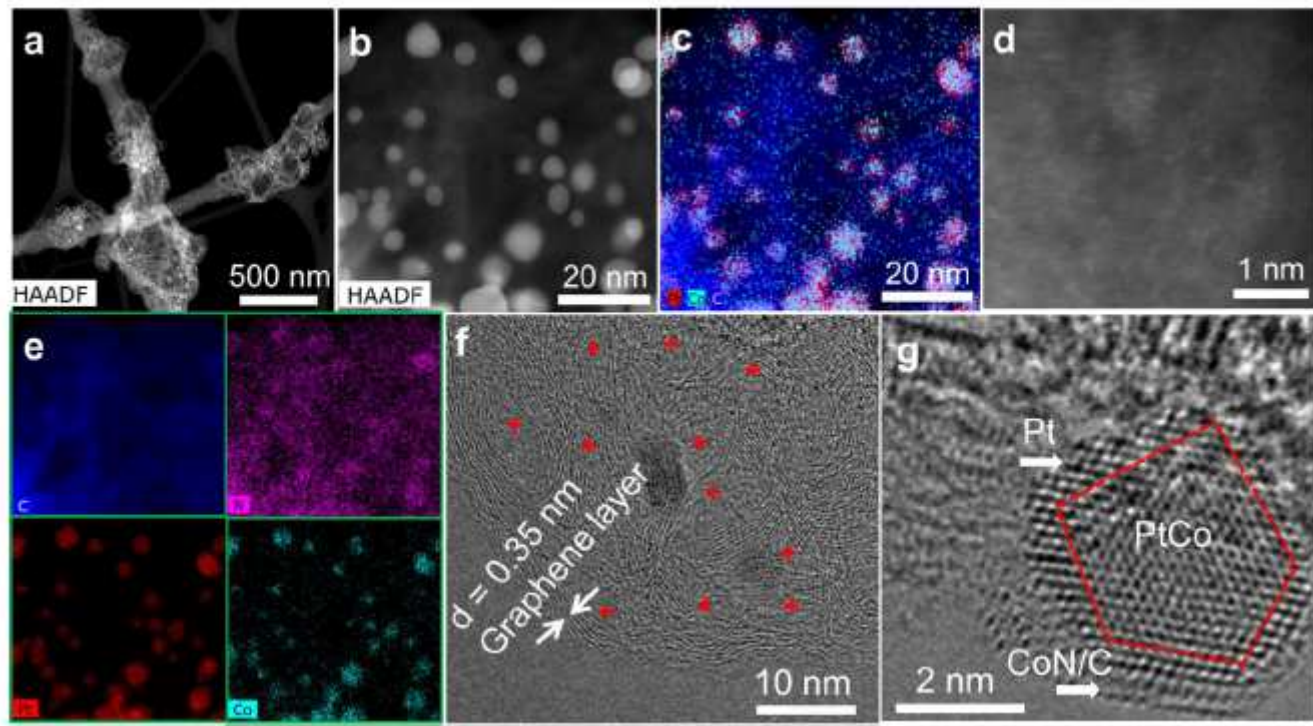


Figure 2

Morphology characterization of LPCNGF. a HAADF-STEM image of two single fibers. b HAADF- STEM image of Pt-Co alloy NPs in LPCNGF. c, e the corresponding EDS elemental mapping. d Atomic-resolution HAADF-STEM image of isolated single Co atoms distributed across the carbon surface. f HRTEM image of carbon from “beads”, showing curved thin graphene layer. g HRTEM image of a representative Pt-Co alloy NP with ordered PtCo core and Pt shell partially covered by CoN/C terraces.

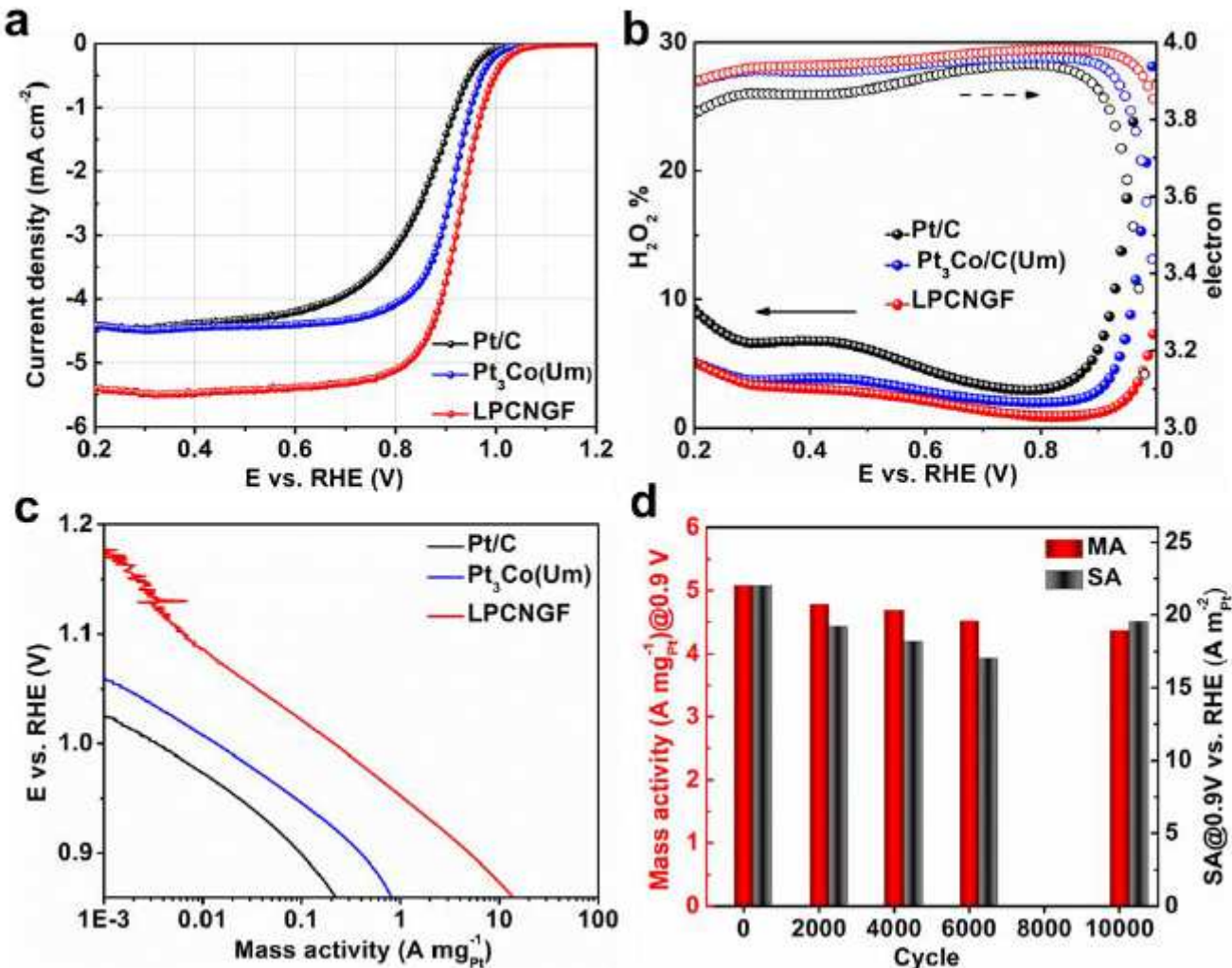


Figure 3

Electrochemical performance evaluation of LPCNGF by the RRDE method. a Steady-state ORR polarization plot of LPCNGF catalyst recorded at a scan rate of 10 mV s⁻¹ and 1600 r.p.m in O₂ saturated 0.1 M HClO₄ electrolyte, and compared with that of 20 wt.% Pt/C and 30 wt.% Pt₃Co/C(Um). Pt loading is ~ 4 $\mu\text{gPt cm}^{-2}$ for LPCNGF, ~ 80 $\mu\text{gPt cm}^{-2}$ for Pt/C and ~ 14 $\mu\text{gPt cm}^{-2}$ for Pt₃Co/C(Um). b The corresponding H₂O₂ yield and electron transfer number. c The corresponding MA Tafel plots. d MA and SA as function of cycle number by RRDE

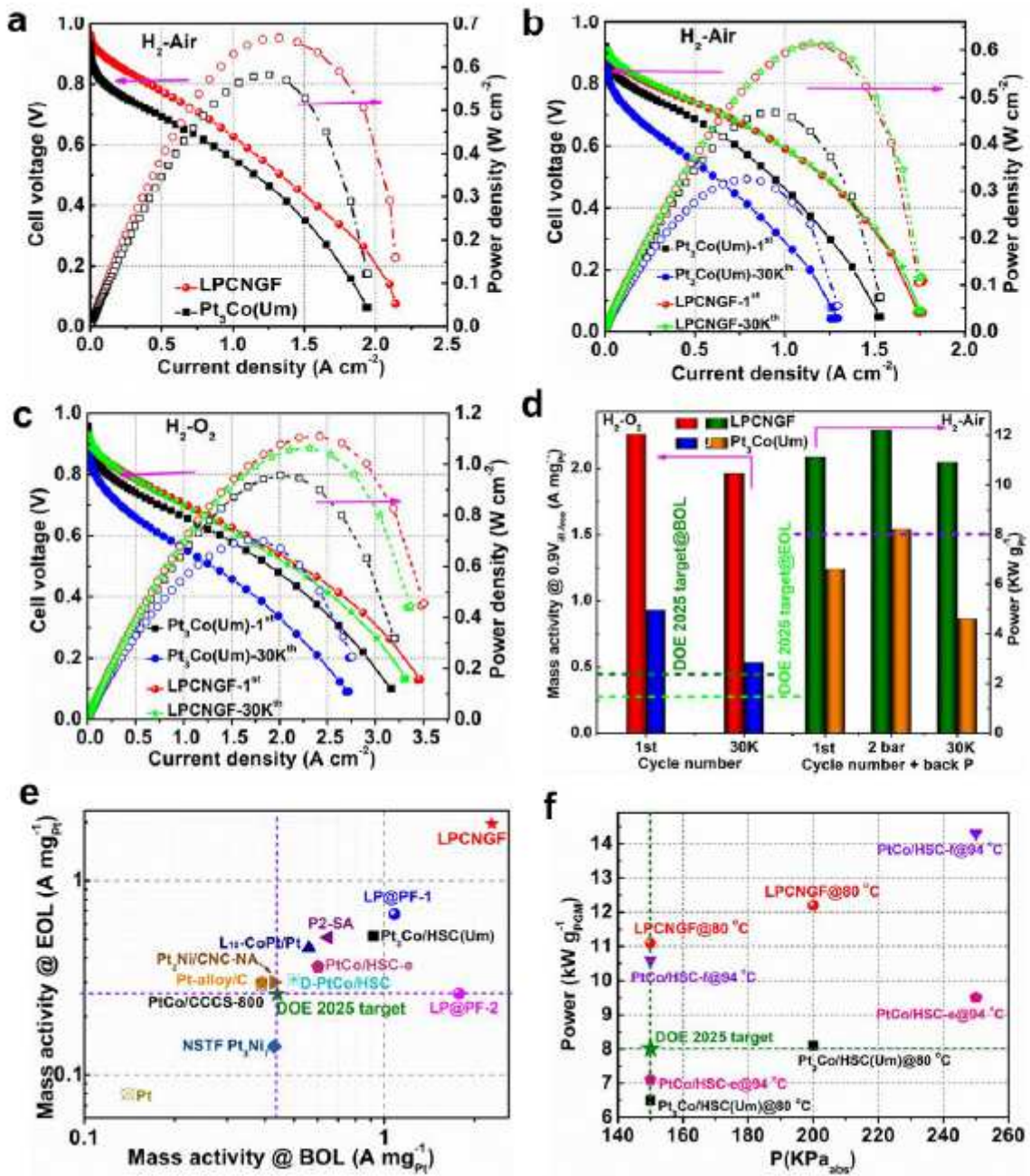


Figure 4

PEMFC performance and durability evaluation of LPCNGF. a H₂-Air fuel cell polarization and power density plots of LPCNGF under $\text{Pa}=\text{Pc}=200 \text{ kPa}_{\text{abs}}$. MEA with 30 wt.% $\text{Pt}_3\text{Co}(\text{Um})$ as cathodic catalyst was tested under the same condition as benchmark. b H₂-Air fuel cell i-v polarization and power density before and after 30 000 cycles AST test under $\text{Pa}=\text{Pc}=150 \text{ kPa}_{\text{abs}}$. c i-v polarization and power density for the same MEA with LPCNGF catalyst in a continued 30 000 AST test in a H₂-O₂ fuel cell after test in (b). d fuel cell MA at 0.9 ViR-free and power per gram of Pt before and after 30 000 AST. e MAs of different catalysts at 0.9 ViR-free before and after 30 000 AST in PEMFC. Catalysts include those from this work and previous reported ones: LP@PF-1/24, L10-CoPt/Pt31, P2-SA32, NSTF Pt₃Ni733, Pt2Ni/CNC-NA34, PtCo/HSC-e35, Pt-alloy/C and Pt3, PtCo/CCCS-80036. f power per gram PGM of

catalysts from this work and the previous reported³⁵. For all the fuel cell tests, membrane = Nafion 211, temperature = 80 oC, cathode loading \leq 0.056 mgPt cm⁻², anode loading \leq 0.035 mgPt cm⁻², R_{Ha} = R_{He} = 100 %. For H₂-Air cell, PH₂ = PAir = 150 kPaabs or 200 kPaabs; H₂ flow rate = 200 ml min⁻¹, and air flow rate = 780 ml min⁻¹; for H₂-O₂ cell, PH₂ = PO₂ = 150 kPaabs, H₂ flow rate = O₂ flow rate = 200 ml min⁻¹.

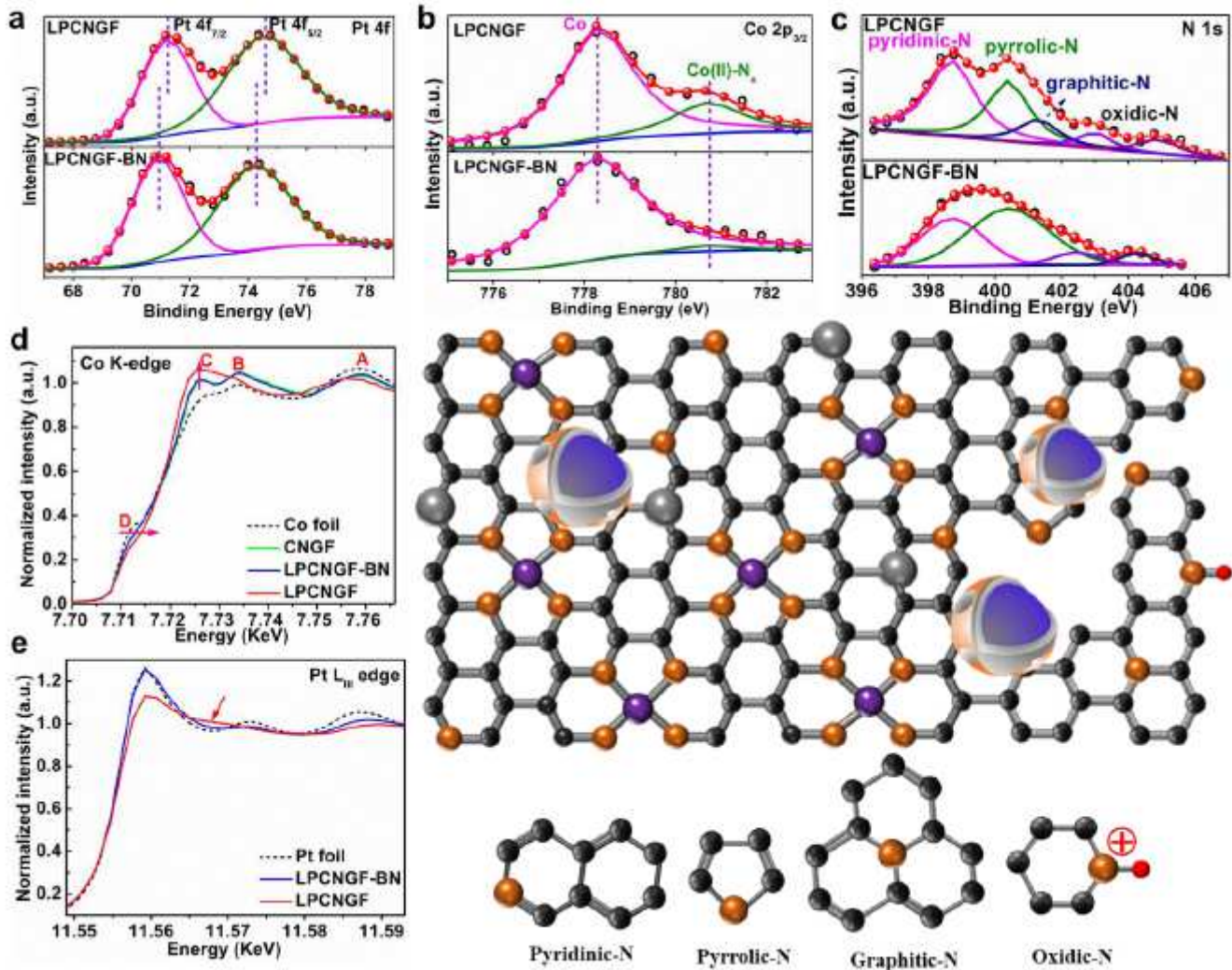


Figure 5

Structural characterization of the LPCNGF catalyst. XPS spectra of a Pt 4f, b Co 2p_{3/2} and c N 1s binding energy before (-BN) and after NH₃ treatment. XANES spectra at d Co K-edge and e Pt L_{III}-edge before and after NH₃ treatment with the metal foil as reference. f, Schematic illustration of LPCNGF structure.

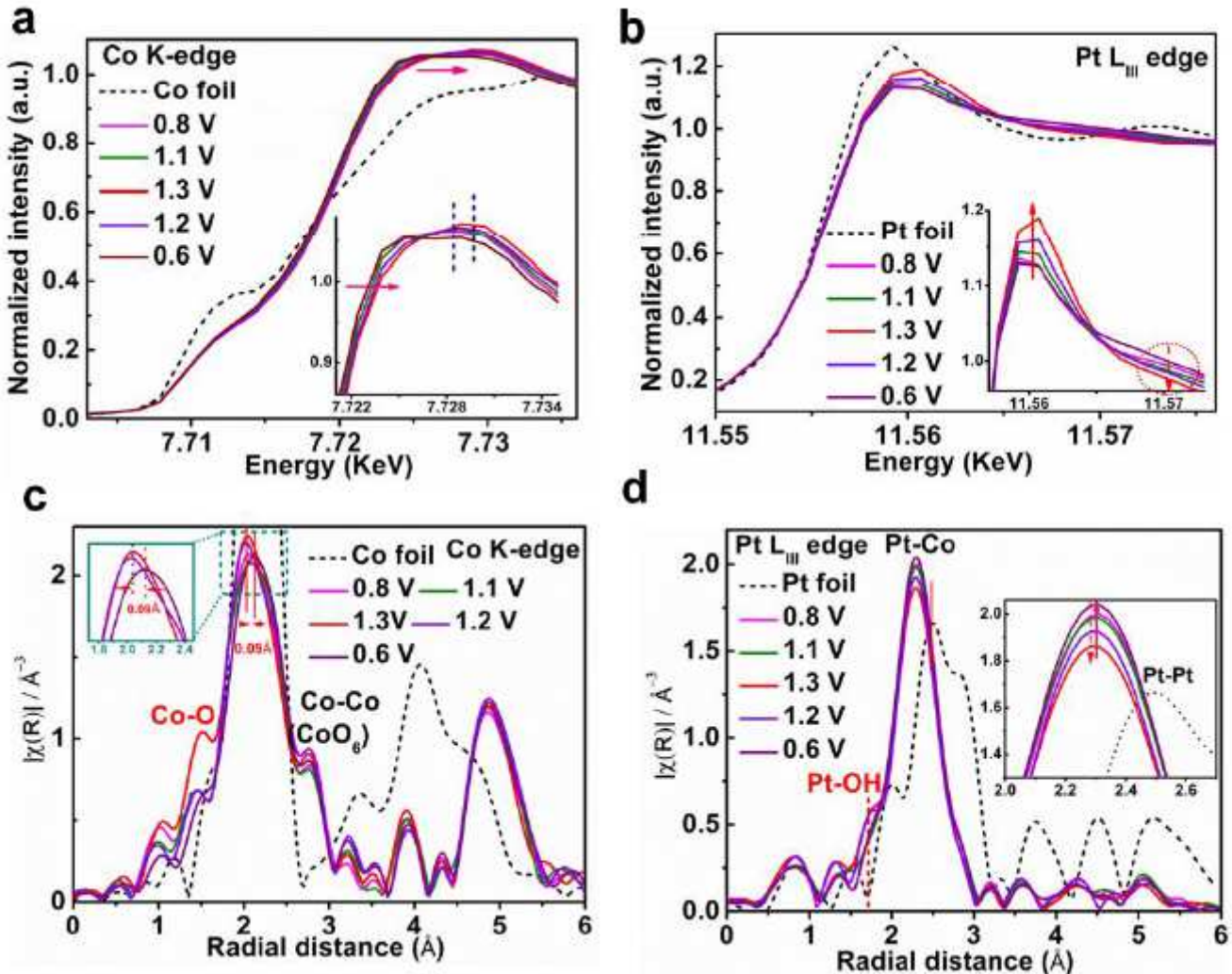


Figure 6

In-situ X-ray absorption spectra of LPCNGF. a Co K-edge and b Pt L_{III}-edge XANES spectra measured at different potentials ascending from 0.8 V, 1.1 V to 1.3 V and then descending to 1.2 V and 0.6 V in O₂ saturated 0.1 M HClO₄ electrolyte. Insets magnify the WL region, clearly showing structure evolution during the ORR process. FT EXAFS spectra at c Co K-edge and d Pt L_{III}-edge collected at potentials ascending from 0.8 V, 1.1 V to 1.3 V and then descending to 1.2 V and 0.6 V in O₂ saturated 0.1 M HClO₄ electrolyte. Insets are enlargements of c Co-Co and d Pt-Co peaks.

Supplementary Files

This is a list of supplementary files associated with this preprint. Click to download.

- [SupplementaryInformationLC.pdf](#)